

APPLYING INFRARED THERMOGRAPHY AS A METHOD FOR ON-LINE MONITORING OF TURBINE BLADE COOLANT FLOW

Eric T. DeShong, first author*

Department of Mechanical Engineering, Pennsylvania State University
3127 Research Drive
State College, PA 16801
etd5060@psu.edu

Benjamin Peters, second author

H. Milton Stewart School of Industrial and Systems Engineering, Georgia Institute of Technology
755 Ferst Drive
Atlanta, GA 30332
bpeters9@gatech.edu

Kamran Paynabar, third author

H. Milton Stewart School of Industrial and Systems Engineering, Georgia Institute of Technology
436 Groseclose Building
Atlanta, GA 30332
kamran.paynabar@isye.gatech.edu

Nagi Gebraeel, fourth author

H. Milton Stewart School of Industrial and Systems Engineering, Georgia Institute of Technology
320 Groseclose Building
Atlanta, GA 30332
nagi.gebraeel@isye.gatech.edu

Karen A. Thole, fifth author

Department of Mechanical Engineering, Pennsylvania State University
3127 Research Drive
State College, PA 16801
kthole@psu.edu

Reid A. Berdanier, sixth author

Department of Mechanical Engineering, Pennsylvania State University
3127 Research Drive
State College, PA 16801
rberdanier@psu.edu

* Corresponding author

ABSTRACT

As gas turbine engine manufacturers strive to implement condition-based operation and maintenance, there is a need for blade monitoring strategies capable of early fault detection and root cause determination. Given the importance of blade cooling flows to turbine blade health and longevity, there is a distinct lack of methodologies for coolant flow rate monitoring. The present study addresses this identified opportunity by applying an infrared (IR) thermography system on an engine-representative research turbine to generate data-driven models for prediction of blade coolant flow rate. Thermal images were used as inputs to a linear regression and regularization algorithm to relate blade surface temperature distribution with blade coolant flow rate. Additionally, this study investigates how coolant flow rate prediction accuracy is influenced by the number and breadth of diagnostic measurements. The results of this study indicate that a source of high-fidelity training data can be used to predict blade coolant flow rate within about six percent error. Furthermore, identification of prioritized sensor placement supports application of this technique across multiple sensor technologies capable of measuring blade surface temperature in operating gas turbine engines, including spatially-resolved and point-based measurement techniques.

INTRODUCTION

The typical failure modes for turbine blades are high cycle fatigue, oxidation, sulphidation, hot corrosion, creep, and erosion [1]. Turbine components are more susceptible to damage from these failure modes when they are operated at elevated temperatures. Therefore, blade metal temperature is a driving factor affecting the longevity of gas turbine blades. Specifically, this relationship has been approximated as a 50 percent life reduction when blade temperature increases by 25 to 40 °C [2–4].

In modern engines, the main gas path (MGP) temperature entering the turbine can reach 1650 °C (3000 °F). However, turbine airfoils must be kept well below this temperature to avoid damage via identified failure modes. To accomplish this task, lower temperature fluid is diverted from the compressor to cool the turbine hardware using complex cooling configurations, including internal cooling passages outfitted with heat transfer augmentation features and film-cooling holes that deliver cooling flow to the external blade surface. Together, these internal and external cooling features result in a cooling effectiveness for modern turbine airfoils of about 60% [5], which shows the reliance of turbine airfoils on cooling flows for maintaining health and longevity.

Given the importance of cooling flows to the long-term durability of turbine hardware, there is a substantial opportunity for cost savings if on-line monitoring of coolant flow can be integrated into a condition-based monitoring approach. For example, this type of condition-based operation and maintenance (CBOM) strategy can reduce unscheduled downtime, which costs liquefied natural gas facilities around \$25 million per day [6]. In addition to reducing unscheduled downtime, CBOM can potentially eliminate the need for inspection downtime, which is scheduled to occur every 12,500 engine hours in some applications [7]. For engine manufacturers and operators to realize these potential financial savings, there is a requirement for the development of novel methods for on-line diagnostics and prognostics.

LITERATURE REVIEW

Despite the importance of blade cooling flow to blade health and longevity, the blade health monitoring methods described in the open literature do not directly monitor characteristics of the blade coolant. Instead, the majority of existing blade health monitoring techniques detect geometrical [8,9], structural [10–14], or aerodynamic performance [15] degradation using blade tip timing [12,13,15–19], blade tip clearance [15,20], vibration [9,13–15], high-resolution shaft speed [21], fast-response pressure [8,11,15], and gas path analysis [22] sensors. In the turbine section, thermal barrier coatings (TBC) and external film cooling flows are used to shield the blade hardware from the hot MGP flow. Therefore, in the pursuit of early detection and root cause determination of blade degradation, there is a need for dedicated monitoring of TBCs and blade cooling flows.

Although no studies have addressed blade coolant monitoring, a few studies have shown capability for TBC monitoring with demonstration on operating gas turbine engines. LeMieux [23] showed a major step forward in blade health monitoring by applying an infrared thermography camera on a Westinghouse 501FD power generation gas turbine engine for continuous, real-time TBC monitoring. The monitoring system was able to successfully image 85 percent of the blade surface during engine operation at 3,600 revolutions per minute (rpm). Furthermore, the system was successfully operated for over 8000 engine hours. In their report, LeMieux stated that the TBC monitoring system would be available on Siemens next generation gas turbine engines, and that retrofits were being offered to customers with existing Siemens engines. In a similar study, Markham et al. [24] demonstrated IR blade imaging capability on a commercial aviation gas turbine engine operating at over 10,000 rpm for the purpose of TBC performance monitoring and cooling design evaluation.

In addition to infrared thermography, there are a number of methods available for quantifying blade surface temperature in an engine environment. Understanding the capabilities of each measurement technique is important for interpreting their respective utility to blade coolant monitoring. In general, blade temperature measurement technology can be separated into two groups: contact and non-contact methods. Contact methods, like thermocouples [25,26], thin-film resistance temperature devices [27–30], and fiber optic sensors [31] are typically used in research and engine development environments, and therefore are not currently applicable to long-term blade health monitoring in the hot section of operating engines. Non-contact measurement methods are more feasible for long-term use in the hot section of engines because they can be installed outside of the hot MGP on stationary hardware. Non-contact measurement methods that have been used in engine-relevant environments include thermographic phosphors, pyrometry, and IR thermography.

The thermographic phosphor measurement method involves coating the target surface with a phosphorescent layer. By exciting the phosphors with ultraviolet light, the temporal rate of decay of luminescence can be related to the surface temperature [32]. This method has been used for blade temperature measurement in an operating engine [33], and it is well suited for use with TBC-coated surfaces because the phosphorescent particles can be integrated directly into the TBC layer [34].

Radiation pyrometry measures radiant energy emitted from a surface. The target surface temperature can be accurately measured based on a known target surface emissivity, assuming contributions of reflected radiation can be minimized or accounted for in the pyrometer calibration. Fundamentally, pyrometers are point measurements, although in some applications the focal area can be scanned across a surface to capture spatial temperature variation [35,36]. Given their simplicity and durability, there are numerous examples of pyrometer utilization in realistic engine environments [37–39].

IR thermography is a two-dimensional form of pyrometry by which radiant energy is directed onto a focal plane array. The result is a thermal image with resolution equal to the matrix size of the focal plane array. Despite the increased complexity of IR thermography systems relative to pyrometers, there are numerous examples of IR imaging of rotating blades [24,40–42]. Results from Markham et al. [24], Christensen et al. [41], and Knisely et al. [42] specifically show that state-of-the-art thermal imaging systems can reliably capture small features on the blade surface.

Cumulatively, the list of methods available for quantifying blade surface temperature for long-term blade health monitoring applications comprises these three methods. Their differences in cost, complexity, and capability dictates their applicability to the blade coolant monitoring technique developed in the subsequent sections, which relates the blade temperature distribution to the blade coolant flow rate.

FACTORS AFFECTING BLADE SURFACE TEMPERATURE

One of the difficulties associated with relating cooling flow rate (\dot{m}_{cool}) to blade surface temperature (T) is the large number of parameters that affect the surface temperature of a modern, highly-cooled gas turbine blade. To illustrate this point, Figure 1 shows a 1D approximation of the heat transfer through a film-cooled turbine blade wall with negligible radiative heat transfer. This 1D analysis informs the identification of the numerous independent parameters affected the blade surface temperature, which is relevant to the determination of the data sets required for training the diagnostic model.

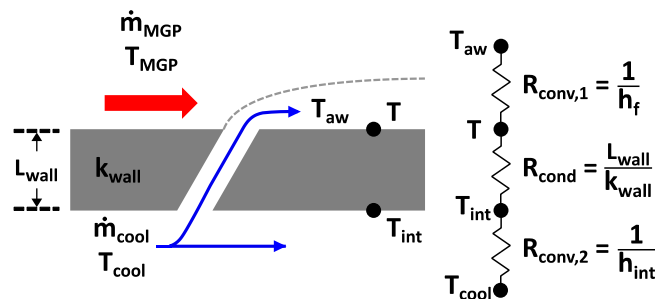


Figure 1. Simplified 1-dimensional analysis of film-cooling heat transfer.

In the presented analysis, the major difficulty is determining the internal and external heat transfer coefficients, which ultimately depend on numerous geometric, thermal, and fluid dynamic parameters. The functional relationship between blade surface temperature and the parameters from Figure 1 is shown in Eq. (1),

$$T = f\left(\begin{array}{l} T_{MGP}, T_{cool}, \dot{m}_{MGP}, \dot{m}_{cool}, \text{ geometry, rotation} \\ \text{thermal state, material and fluid properties} \end{array}\right) \quad (1)$$

where T_{MGP} is the temperature of the main gas path flow, T_{cool} is the blade coolant temperature, \dot{m}_{MGP} is the main gas path flow rate, and \dot{m}_{cool} is the blade coolant flow rate. This functional relationship was used to guide both the experimental design and the modelling strategies used for prediction of \dot{m}_{cool} .

Because the effects of each parameter are complex, this study has implemented a data-driven modelling approach. Using this approach, the breadth of parameters captured in the training data roughly determines the limitations of the model. For this reason, each parameter in Eq. (1) is discussed here in terms of its inclusion or exclusion as an independent variable in the data set used to train and test the model. The consequences of these decisions on model application are described as well.

The two primary independent variables in this study were T_{MGP} and \dot{m}_{cool} . Figure 2 shows the data set used in this study for modelling in terms of T_{MGP} (abscissa) and \dot{m}_{cool} (ordinate), where each point indicates conditions at which IR measurements were collected. As the high temperature driver of heat transfer to the blade, T_{MGP} is expected to have a substantial influence on the blade surface temperature distribution. For this reason, large T_{MGP} variations were included in the data set, enabling the predictive model to account for T_{MGP} and adjust \dot{m}_{cool} predictions accordingly; this process reduces errors caused by T_{MGP} volatility in a real-world application. In total, four T_{MGP} set points were measured spanning 14% of the maximum T_{MGP} across all cases. As the primary parameter of interest, large variations in \dot{m}_{cool} were also included in the data set. Five distinct flow rates were investigated between 25% and 100% of the maximum \dot{m}_{cool} across all cases. To illustrate the dependence of blade temperature on these two driving parameters, each point in Figure 2 is colored to reflect the area-averaged blade temperature – as measured by the IR camera - with dark blue and dark red representing the low and high temperature extrema, respectively. Generally, point colors transition from blue in the top left corner – where T_{MGP} is lowest and \dot{m}_{cool} is highest – to red in the bottom right corner – where T_{MGP} is highest and \dot{m}_{cool} is lowest.

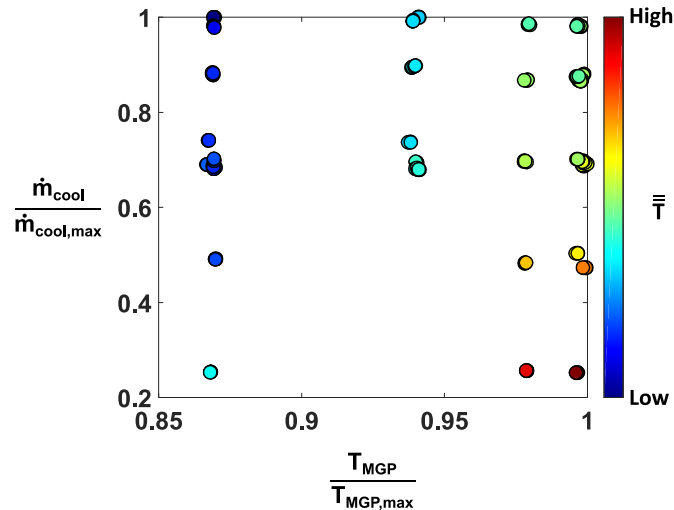


Figure 2. Distribution of T_{MGP} and \dot{m}_{cool} conditions at which blade temperature measurements were collected for predictive modelling of \dot{m}_{cool} .

In addition to the selected primary parameters, small variations in some of the other parameters in Eq. (1) were included to mimic real-world engine operation. Specifically, T_{cool} , dT_{ID}/dt , and dT_{OD}/dt were allowed to vary slightly amidst the larger variations to T_{MGP} and \dot{m}_{cool} . The variation of these secondary parameters mimics boundary condition and engine operating mode variability typically experienced in real-world engine operation. In Figure 2, the dependence of blade temperature on the secondary parameters is evidenced by color variations within point clusters. The remainder of the parameters in Eq. (1) were either held constant across the experimental data set or not controlled directly. In particular, \dot{m}_{MGP} , geometry, and rotating speed were held constant across all cases. Table 1 describes the non-dimensional parameters relevant to the operation of the turbine.

Table 1. Turbine Operation Non-Dimensional Parameters

Parameter	Value
Vane inlet Mach number	0.1
Vane inlet axial Reynolds number	$8.8 \times 10^4 - 1.0 \times 10^5$
Blade inlet axial Reynolds number	$8.5 \times 10^4 - 9.9 \times 10^4$
Rotational Reynolds number	$2.7 \times 10^6 - 3.4 \times 10^6$
Coolant-to-MGP density ratio	1.5 – 1.7

In summary, by setting the turbine parameters as indicated, the turbine is operated at or near a single aerodynamic condition, which inherently tailors the resulting model to a discrete monitoring application. In discrete monitoring, predictions are generated only at a single operating point. The model in this study can predict \dot{m}_{cool} and T_{MGP} , and any changes to these parameters outside of their healthy range can be recognized, which indicates the root cause of changes to blade surface temperature as occurring in either the secondary air or combustion systems, respectively.

EXPERIMENTAL METHODS

The training and testing data sets were generated at the Steady Thermal Aero Research Turbine (START) Laboratory at Penn State University. This facility operates continuously at engine-relevant aerothermal conditions using turbine geometries that are representative of the current state-of-the-art for a commercial aviation gas turbine engine. A detailed description of the START facility was given by Barringer et al. [43], and an abbreviated description is provided here.

The main components of the system relevant to this study are the two industrial compressors, a natural gas combustion chamber to heat the MGP flow, a heat exchanger to lower the temperature of the cooling flows, the one-stage turbine test section, and a water-brake dynamometer for speed control and power extraction. The two compressors (1.1 MW, 1500 hp) continuously draw in ambient air at a combined flow rate of up to 10.4 kg/s (25 lb_m/s). Flow exits the compressors at approximately 480 kPa (70 psia) and 110 °C (230 °F). The majority of the compressor exit flow enters the MGP and is directed into the inlet of the in-line natural gas heater chamber. The MGP temperature can be raised to a maximum temperature of 400 °C (750 °F), although the MGP temperatures in this study were lower. The remainder of the compressor exit flow is diverted through a shell-and-tube heat exchanger to reduce its temperature to about 0 °C (32 °F). This cold flow is separated into three individual flows: blade cooling flow, vane trailing edge cooling flow, and purge sealing flow. In this particular study, only blade cooling flow was used. These MGP and cooling flows recombine in the test section, which is a true-scale single-stage turbine. After the test section, an in-line torque meter and a laser tachometer measure shaft torque and speed, respectively. Finally, a shaft-end water-brake dynamometer extracts power and controls turbine rotating speed to within ± 10 rpm of the desired set point.

A representative cross-section view of the turbine test section is shown in Figure 3. Stationary hardware is shown in light grey, and rotating hardware is shown in dark grey. The MGP travels from left to right through the turbine vanes and blades. The blade coolant is pre-swirled prior to entering the disk, where it is routed through the blade-disk attachment into the blade root. The blade coolant continues through internal passageways in the blade before ejection through film-cooling holes onto the blade surface (not shown in Figure 3). It should be noted that a small portion of the supplied blade coolant flow leaks into the wheelspace cavity and eventually egresses through the rim seal into the MGP fluid stream. However, due to the measured thermal state of the rim seal hardware in this study, it is expected that the split of supplied cooling flow between the rim seal and the blade row was constant across all data collected and used for modelling. Measurements of \dot{m}_{MGP} were collected using a Venturi flow meter, and T_{MGP} was measured just prior to the vanes by six circumferentially-distributed temperature probes. Measurement of \dot{m}_{cool} was executed using a Venturi flow meter located upstream of the test section, and T_{cool} was measured by circumferentially-distributed thermocouples located immediately upstream of the pre-swirler vanes. The uncertainty of these temperature and flow rate measurements can be sourced from Berdanier et al. [44].

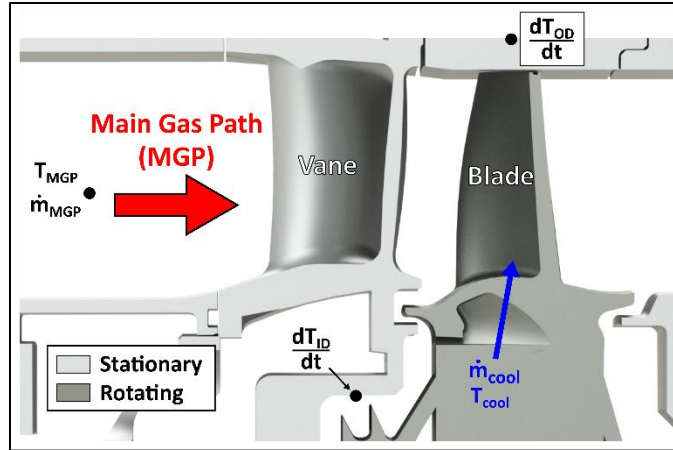


Figure 3. Single-stage turbine cross-section with identified measurement locations.

As shown in Eq. (1), the thermal state of the turbine hardware has an effect on the blade surface temperature, which necessitated the use of additional temperature measurements to quantify the hardware temperature over time. Therefore, thermocouples were installed on the outer-diameter hardware (T_{OD}) and on the inner-diameter hardware (T_{ID}) to approximate the cumulative temperatures of the test-section hardware. The time rate-of-change for these temperatures (dT/dt) was calculated at instances corresponding to IR blade temperature measurements and the resulting outputs were used as potential covariate features for model development. Here, a covariate describes any parameter that has a non-negligible effect on model performance, but is neither the main diagnostic measurement nor the target of predictive modelling.

The main diagnostic parameter used in this study was the spatially-resolved blade surface temperature measured using an IR thermography system. The camera integration, calibration, and operation was introduced in detail by Knisely et al. [42], and the specific information relevant to this study is given here.

The IR camera in this study utilizes a Sofradir MiTIE MARS LW camera engine that contains a HgCdTe (MCT) IR detector, which measures radiant energy in the long wave IR spectrum. The integration time (response time), which is the amount of time required for the camera to capture an image, is adjustable down to $0.6 \mu\text{s}$. For this particular study, the integration time was set at $2 \mu\text{s}$, which was the optimal time that minimized the combined detrimental effects of spatial noise and image blur caused by blade rotation during image capture. With this short integration time, it was necessary to collect and then average consecutive images of the same blade to reduce measurement noise; fifty images were averaged to generate a single blade temperature distribution for this study. Average images were further processed with binning and 3×3 median filtering, which were shown by Knisely et al. [42] to reduce measurement errors due to striping and nonresponsive pixels.

A calibration plate was used to perform external calibration of the IR system [42] across a range of surface temperatures following the procedure detailed by Mori et al. [45]. After calibration, the camera was installed on the test turbine and used to measure rotating blades. For this study, only one location on one blade was measured for consistency. The target blade was prepared with a high emissivity coating, which helped to improve measurement accuracy by reducing the contributions from background sources of radiant energy. The target surface of the blade was imaged by the IR camera at approximately a 25° viewing angle relative to the surface normal direction. The temperature measurement uncertainty of the IR camera, when non-dimensionalized by $T_{MGP,max}$, was determined to be 0.62% for the conditions examined in this study.

The probe access and a representative view of the IR camera onto the blade surface is shown in Figure 4(a). The camera optics were integrated through the body of an additively-manufactured vane, which enabled imaging of the pressure side of the blades. Although the system was able to image the entire pressure side of the blades, only a small region downstream of four diffuser-shaped film-cooling holes was selected for this study. An example of a post-processed thermal image, Figure 4(b), shows the pitchwise (z -direction) periodic temperature variation caused by the row of film-cooling holes. The amplitude of these periodic temperature fluctuations is greatest immediately downstream of the film-cooling holes, and decreases with increasing downstream distance as the coolant becomes more evenly distributed along the blade surface. There is also a slight pitchwise temperature gradient, likely caused by the internal coolant temperature increasing in the z -direction from the blade root towards the blade tip. The z -direction temperature gradient is observed consistently across all images collected for this study, so it can be considered a result of the blade design that will be inherently captured by the data-driven modelling process.

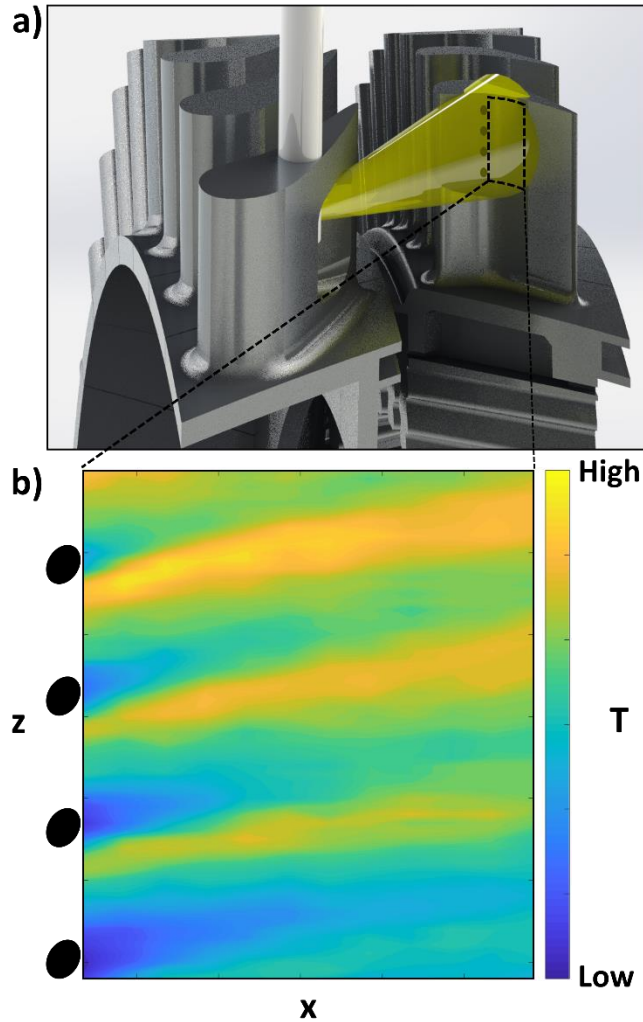
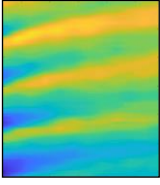
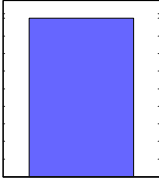
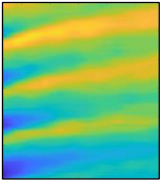
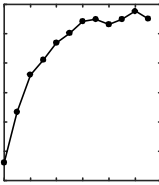
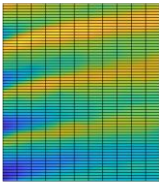


Figure 4. IR camera a) integration and blade view, and b) example thermal image.

PREDICTIVE MODEL DEVELOPMENT METHODS

For diagnostic measurements that exhibit high temporal or spatial resolution, it is common to perform feature extraction to reduce the overall size of the candidate feature set with minimal loss of information. The thermal images analyzed in this study represent 756 individual pixel temperature measurements. These individual temperatures can be used directly as features, or statistical representations of the temperature measurements can be used as unique features with reduced dimensionality and complexity. In the end, three types of features were investigated to assess the tradeoff between feature dimensionality and prediction accuracy. Each type of feature is shown in Table 2 for the example image shown in Figure 4(b).

Table 2. Predictive Modelling Features

Feature	Process	Result
2D Average \bar{T}	Avg 	
Pitchwise Average $\bar{T}(x)$	Avg 	
Image $T(x,z)$	N/A	

The first type of feature in Table 2 is generated by computing the two-dimensional average of the IR image, \bar{T} , which results in a single scalar feature. This type of feature is analogous to the blade temperature measured by a pyrometer with a focal area equivalent to the spatial domain of the IR image shown in Figure 4(b). The second type of feature was generated by calculating the pitchwise average of the IR image, $\bar{T}(x)$, which yields a one-dimensional array of features. This second approach is correlated to the pitchwise-averaged cooling effectiveness, which is typically used in the study of film-cooling performance to understand cooling as a function of downstream distance. The third and last type of feature examines individual pixels in the IR image as unique potential predictors of \dot{m}_{cool} , which makes this type of feature truly two-dimensional. In Table 2, the grid overlay for the two-dimensional data, $T(x,z)$, shows the image resolution, where each grid intersection corresponds to a pixel temperature measurement.

After each type of feature set was curated, predictive modelling was performed using the Least Absolute Shrinkage and Selection Operator (LASSO) [46] regression. LASSO was selected for this application because it has the ability to generate sparse and easily-interpretable models from large and complex data sets [47–50]. Equation (2) shows the optimization problem for LASSO regression for this application,

$$\min_{\beta_0, \beta} \frac{1}{2n} \sum_{i=1}^n (\dot{m}_{cool,i} - \beta_0 - x_i^T \beta)^2 + \lambda \|\beta\|_1 \quad (2)$$

where $\dot{m}_{cool,i}$ is the i th measured blade coolant flow rate in the training set, x_i is the i th set of predictors from the IR images, λ is the tuning parameter, and β is a set of model coefficients. The second term in Eq. (2) is the penalty term that performs both regularization and feature selection, where the selected features correspond to non-zero β coefficients. The tuning parameter, λ , which determines the extent of regularization, was determined using K-Fold Cross Validation with ten folds. The performance of the models generated by LASSO were compared based on their prediction root-mean-square error,

$$RMSE(y) = \sqrt{\frac{\sum_{i=1}^n (y_{pred,i} - y_{meas,i})^2}{n}} \quad (3)$$

where y_{pred} is the predicted parameter of interest, y_{meas} is the measured parameter of interest, and n is the number of predictions. RMSE results will be reported separately for predictions of both \dot{m}_{cool} and T_{MGP} .

For purposes of addressing predictive model stability in the presence of turbine operability variations, two separate data sets were used for model generation. These two data sets were used to evaluate the importance of including covariates in the model, where potential covariate parameters in this study are T_{MGP} , T_{cool} , dT_{ID}/dt , and dT_{OD}/dt . These covariate parameters were selected because they can influence the blade temperature at constant MGP temperature and coolant flow rate conditions, which in turn can lead to increased prediction error. The ISOLATED data set is representative of data generated in an idealized environment at near steady-state conditions ($dT_{\text{ID}}/dt = dT_{\text{OD}}/dt \approx 0$) with tightly-controlled T_{cool} . Aside from \dot{m}_{cool} , T_{MGP} was the only parameter exhibiting large variations in the isolated data set, meaning there was an option to manually include T_{MGP} in the model as a covariate parameter. The secondary parameters were not included as covariates when modelling with the ISOLATED data set because they were tightly controlled during test operations.

The ISOLATED data set was then expanded to include additional data with larger fluctuations of T_{cool} , dT_{ID}/dt , and dT_{OD}/dt to facilitate the consideration of including secondary parameter covariates in the model; this larger data set is referred to as the EXTENDED data set. Figure 5 shows the range of T_{cool} , dT_{ID}/dt , and dT_{OD}/dt for the two data sets, where the range is calculated as the difference between the maximum and minimum parameter value across all measured conditions. Here, the range is important to consider rather than the absolute value of each covariate parameter because the breadth of variation is what leads to increased prediction error when training and testing the model. The EXTENDED data set represents nearly a 5x increase of range for T_{cool} , as well as a nearly 2x increase of range for dT_{ID}/dt and dT_{OD}/dt .

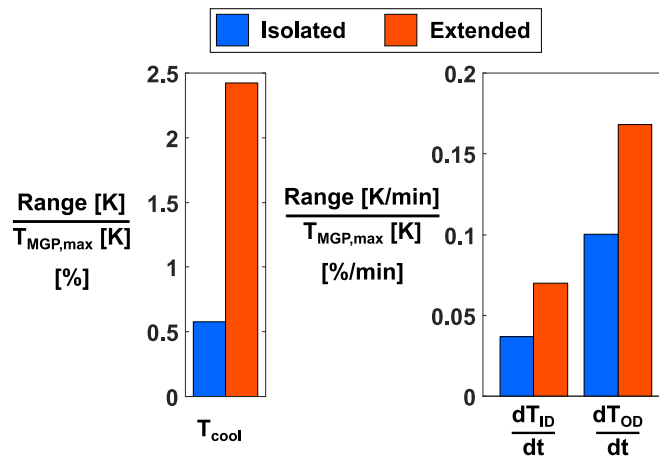


Figure 5. Range comparison of coolant temperature and thermal state parameters between the ISOLATED and EXTENDED data sets.

ANALYSIS OF FEATURE EXTRACTION AND PREDICTIVE MODELLING METHODS

To simplify the analysis, the ISOLATED data set was analyzed first to separate the effects of the primary covariate, T_{MGP} , from the secondary covariates, and the learnings from this idealized test were subsequently applied to the EXTENDED data set. Figure 6 shows the prediction error for \dot{m}_{cool} when applying LASSO to the ISOLATED data set in the solid blue bars. The cross-hatched bars show the prediction error when T_{MGP} is measured by the vane inlet thermocouples and used as a covariate in the model. Figure 6 includes three sets of bars corresponding to the three feature types discussed in Table 2. The height of each bar indicates the median prediction error from 250 modelling iterations non-dimensionalized by the maximum \dot{m}_{cool} across all cases. The modelling iterations were performed to desensitize the interpretation of the results from the randomized data grouping. The range of error results from the individual iterations is indicated by range bars bounding the median, which excludes outliers in accordance with the 1.5x inter-quartile range rule.

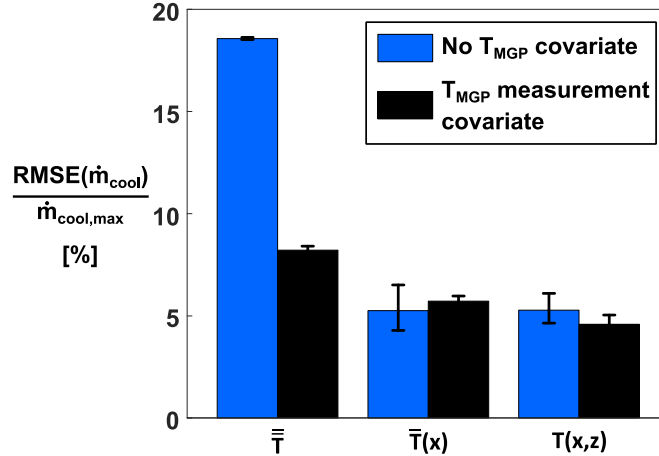


Figure 6. Comparison of coolant flow rate prediction accuracy with and without a priori knowledge of T_{MGP} for each type of feature.

Two key observations can be drawn from Figure 6. First, the $\bar{T}(x)$ and $T(x,z)$ features result in comparable prediction error that is notably lower than the \bar{T} features. This result is expected due to the increased information available for modelling when using the higher dimension features. Second, there is a large improvement to prediction accuracy when using the \bar{T} features if T_{MGP} is measured and used as a covariate during modelling. This drastic improvement – a nearly 50% reduction of prediction error – is not observed for either the $\bar{T}(x)$ or $T(x,z)$ features. Rather, these higher-dimensional features show marginal changes of predictive error magnitude on the order of the iterative range.

The observations associated with Figure 6 raise the question of whether similar improvements to \dot{m}_{cool} prediction accuracy can be realized when using \bar{T} features by first using the IR data to predict T_{MGP} , and then subsequently using the T_{MGP} prediction as a covariate when predicting \dot{m}_{cool} . To address this curiosity, the accuracy of predicting T_{MGP} using only the IR data was examined, and the resulting modelling error is presented in Figure 7. In this scenario, T_{MGP} is the output of the predictive model, rather than a covariate input. The T_{MGP} predictions are highly accurate for all three feature types with errors less than three percent of $T_{MGP,max}$. The $\bar{T}(x)$ and $T(x,z)$ features resulted in T_{MGP} prediction errors less than about one percent of $T_{MGP,max}$. For reference, the reported error for the higher-dimension feature sets is only about two times greater than the typically-quoted error of an un-calibrated K-type thermocouple [51]. The ability to predict \dot{m}_{cool} and T_{MGP} solely using inputs of blade temperature measurements demonstrated in Figure 7 offers noteworthy utility; specifically, it enables root cause determination of turbine blade degradation by decoupling faults associated with secondary air and combustion systems.

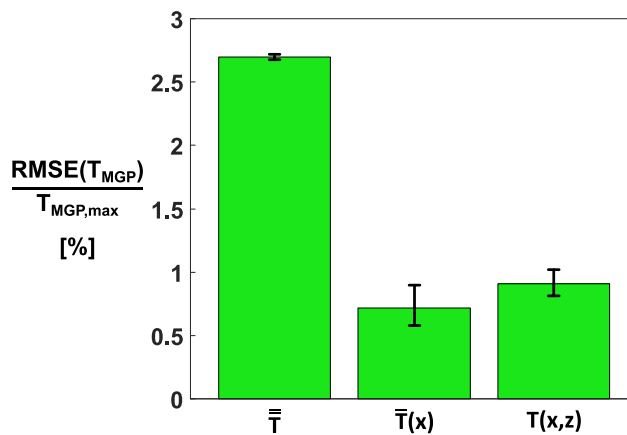


Figure 7. Comparison of T_{MGP} prediction error for each type of feature.

Next, the T_{MGP} predictions were carried forward to the \dot{m}_{cool} prediction by including them as a covariate parameter. These \dot{m}_{cool} prediction error results are shown in Figure 8 alongside the corresponding results for an unknown T_{MGP} . Figure 8 shows there is no benefit to using T_{MGP} predictions as an input to the \dot{m}_{cool} prediction model, and it is actually slightly detrimental when using the $\bar{T}(x)$ or $T(x,z)$ features. Fundamentally, the cause for this result is likely that there is no new information being supplied to the model. The IR data are the root source of all inputs, whether \dot{m}_{cool} is predicted independent from or in conjunction with T_{MGP} . Therefore, it is likely that the original model was already accounting for T_{MGP} without explicitly outputting a T_{MGP} prediction.

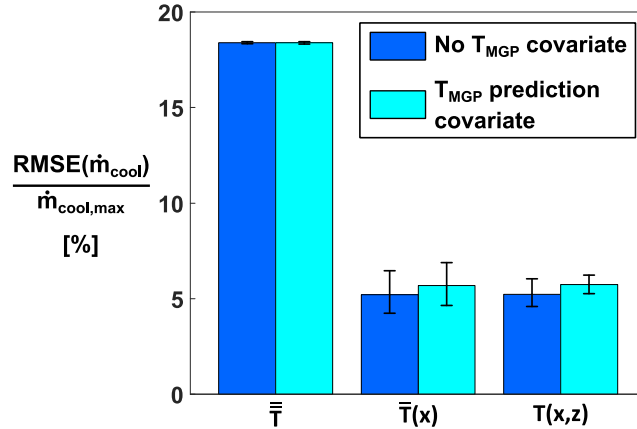


Figure 8. Comparison of coolant flow rate prediction error when modelling is done without T_{MGP} as a covariate, and when T_{MGP} predictions are used as a covariate input to the model.

To this point, the ISOLATED data set has been used to draw two main conclusions: (i) the $\bar{T}(x)$ and $T(x,z)$ features result in the lowest \dot{m}_{cool} prediction errors, and (ii) T_{MGP} should only be used as a covariate if it is known or measured from a sensor other than the main diagnostic measurement source. With these initial conclusions in mind, the analysis approach was translated to the EXTENDED data set to understand implications of more significant variations in T_{cool} , dT_{OD}/dt , and dT_{ID}/dt parameters.

Figure 9 shows the comparison of the \dot{m}_{cool} prediction error results from the ISOLATED and EXTENDED data sets. The blue bars correspond to the ISOLATED dataset, and the orange bars correspond to the EXTENDED data set. Similar to Figure 6, the cross hatched bars indicate there is a priori knowledge of T_{MGP} included in the model as a covariate. Given the similar performance of the $\bar{T}(x)$ and $T(x,z)$ features noted in Figs. 7-9, the remainder of the results will compare only \bar{T} and $T(x,z)$ features for brevity. The preference for $T(x,z)$ features instead of similar $\bar{T}(x)$ features was driven by the potential opportunity for sparse feature selection, which is important for reducing model and measurement system complexity.

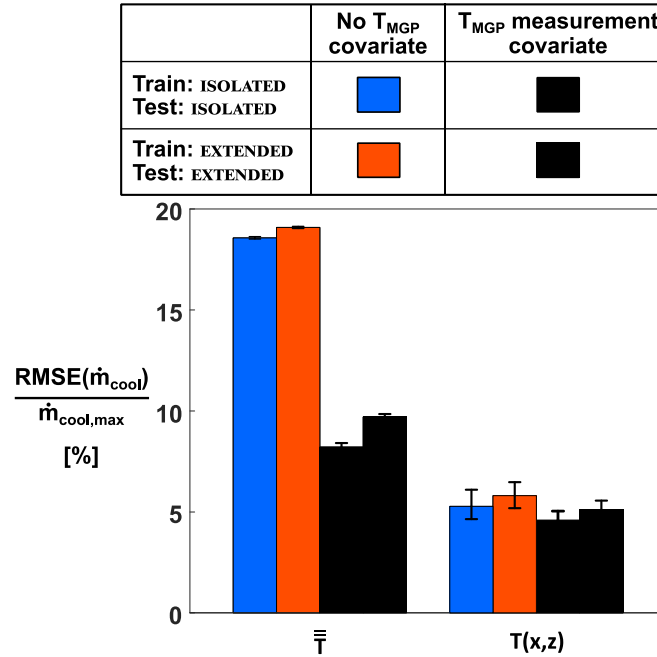


Figure 9. Coolant flow rate prediction error comparison between the ISOLATED and EXTENDED data sets.

As expected, Figure 9 shows that the increased variability of T_{cool} , dT_{ID}/dt , and dT_{OD}/dt has a negative effect on the prediction accuracy of the model – an observation that holds regardless of whether or not T_{MGP} is used as a modelling covariate. This trend is represented by a nearly uniform increase of approximately 2% error for all models. Also from Figure 9, an accuracy improvement is observed for each data set when the T_{MGP} measurement is included as a covariate in the modelling, which agrees with Figure 6. This improvement was more significant for \bar{T} features than $T(x,z)$ features, with prediction error decreasing by a factor of two for each data set.

In the pursuit of higher accuracy when using the EXTENDED data set, models with additional covariates were generated to capture T_{cool} , dT_{ID}/dt , and dT_{OD}/dt variability. Understandably, any benefits of including these parameters as covariates comes at the cost of requiring their measurement in the engine, which can be costly and technically challenging. Figure 10 shows the effect of including these covariate parameters with comparison to the previously reported results.

	T_{MGP} Unknown	T_{MGP} Covariate	T_{cool} , dT_{ID}/dt , and dT_{OD}/dt Covariates	All Covariates
Train: ISOLATED Test: ISOLATED	■	■	N/A	N/A
Train: EXTENDED Test: EXTENDED	■	■	■	■

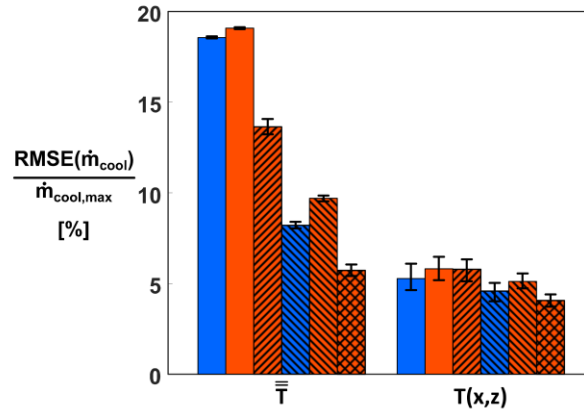


Figure 10. Improvement to blade coolant flow rate prediction error when including coolant temperature and thermal state parameters in the model as covariates.

Figure 10 shows that, when compared to the model with no covariates, the prediction error of the \bar{T} features is greatly reduced by including the additional parameters in the model as covariates. This improvement equates to a reduction of prediction error of about 5% of the maximum coolant flow rate across all cases. When applying the same approach to the $T(x,z)$ features, a negligible improvement was observed. For both data sets, the minimum prediction error, about 6% for \bar{T} features and 4% for $T(x,z)$ features, was achieved by modelling with all covariates. However, the high accuracy of these models comes at the cost of requiring the most physical measurements to serve as model inputs – one for each covariate parameter.

Given the information in Figure 10, it is important to consider the tradeoff between prediction accuracy and sensor requirements to determine which approach is preferable. For the \bar{T} features, the prediction error was decreased by a factor of approximately four when all the covariates were used. Even for engine applications where very few sensors are available and additional sensors are costly, the noteworthy decrease of prediction error may warrant the inclusion of the covariate parameters. For the $T(x,z)$ features, there was only about a 1% decrease to prediction error when using all the covariates. This small improvement to model performance may not warrant the significant effort and investment necessary to measure all the covariate parameters. For this reason, the remainder of the paper will focus on the modelling approach that solely uses $T(x,z)$ features without covariates because it represents the best combination of high accuracy and minimal sensor requirements.

ANALYSIS OF SELECTED FEATURES

Although every pixel of the image was available to LASSO for training the model, only a subset of the pixels were used to generate \dot{m}_{cool} predictions. The number and location of the selected features are important to consider because they dictate the spatial resolution requirements of the sensor used to quantify the blade surface temperature. For example, if the model only uses a few regions in the IR image, then it could be reasonable to use single point sensors as inputs for the predictive model instead of a two-dimensional measurement like IR thermography or thermographic phosphors.

Figure 11 shows the feature selection for the modelling approach in which no covariates were used. Figure 11(a) shows the value of the LASSO model coefficients, β , where non-zero values of β identify selected features in the two-dimensional image space. Within each modelling iteration, the value of the coefficients is constant across all conditions examined in this study (Figure 2). The black lines in Figure 11(a) outline the areas with non-zero coefficients, and the same areas are superimposed on the temperature data contours in Figure 11(b). The connection of model features with spatially-resolved temperature data in Figure 11(b) highlights portions of the image that contain informative content for predicting \dot{m}_{cool} ; the remainder of the IR image is disregarded by the model. Interestingly, the feature selection is sparse, and only two regions are identified as significant with non-zero model coefficients. The

relative locations of the two informative regions are also noteworthy; LASSO independently selected the hottest and coldest locations in the image. These hot and cold regions are close to the trailing edge of the film-cooling holes, where the coolant jets are most distinct from the remainder of the blade boundary layer flow.

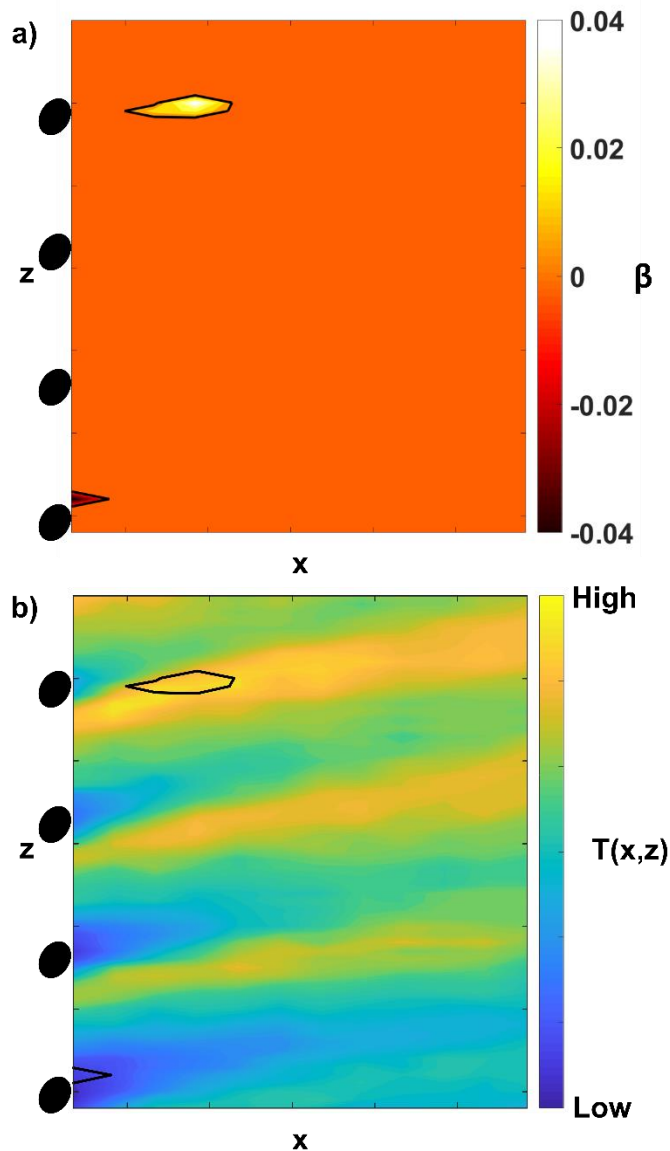


Figure 11. Spatial locations of selected features identified from the a) model coefficients and shown with respect to b) the original IR image.

The selection of hot and cold locations in Figure 11(b) is logical when considering the main factors affecting blade temperature in this experiment. The parameters with the largest variations in the training data (\dot{m}_{cool} and T_{MGP}) have competing effects on blade temperature. Increasing T_{MGP} will drive up blade temperature, while increasing \dot{m}_{cool} will tend to decrease blade temperature. Therefore, the non-zero coefficient region that is associated with T_{MGP} will contain positive coefficients, while the region associated with \dot{m}_{cool} will contain negative coefficients. In other words, the cold zone directly behind a film-cooling hole is highly correlated with \dot{m}_{cool} and minimally correlated with T_{MGP} , whereas the hot zone between film-cooling jets is highly correlated with T_{MGP} and minimally correlated with \dot{m}_{cool} .

Although LASSO only identified two regions with informative features, the model uses all pixels contained within those regions, which means the model uses many more than two features. Based on this observation, a final analysis focused on minimizing the number of features in the identified regions was performed. For this analysis, LASSO was forced to select feature sets of decreasing size.

Figure 12(a) shows the \dot{m}_{cool} prediction error as a function of feature count between one and ten features. Substantial reductions in the median and range of prediction errors are observed up to a feature count of four, beyond which there are diminishing returns for including additional features. Figure 12(b) shows the selected feature positions relative to the IR image for a feature count of four, as identified by the boxed case in Figure 12(a). This low feature count expands the possibilities for sensor options that could be used in the engine to measure these four temperatures. Single point sensors, like a non-contact pyrometer, could be used to focus on each individual location.

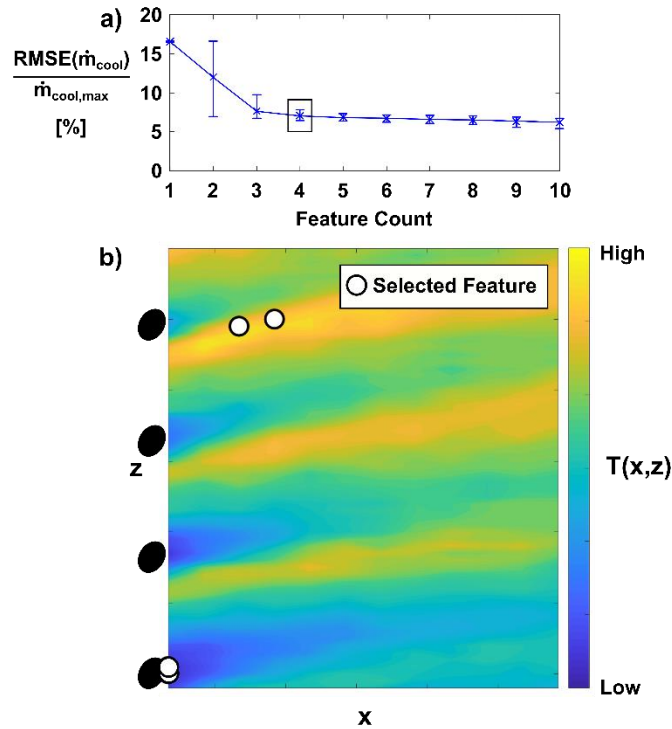


Figure 12. Assessment of decreasing feature counts. (a) Coolant flow rate prediction error as a function of the number of features used in the model and (b) identified locations for four features.

CONCLUSIONS

This study utilized measurements of blade surface temperature collected from an IR camera installed in a one-stage turbine research facility to demonstrate the feasibility of a data-driven model for prediction of blade coolant flow rate. Ultimately, the ability to predict coolant flow rate was demonstrated with a root-mean-square modelling error better than six percent of the maximum flow rate. A further reduction of prediction errors associated with the coolant flow rate model to four percent was achieved by including measurements of T_{MGP} , T_{cool} , dT_{ID}/dt , and dT_{OD}/dt as covariate parameters in the model. As an added benefit, the direct correlation of T_{MGP} with measured blade temperature supported an independent prediction of T_{MGP} with less than one percent error relative to the maximum T_{MGP} across all cases. Cumulatively, these results indicate the predictive capability that can be achieved when a two-dimensional measurement technology, such as infrared thermography, is used as the main diagnostic measurement.

To investigate the accuracy tradeoff when using a single-point sensor, such as a pyrometer, various averaging and feature selection techniques were utilized. First, the thermal images were spatially-averaged to generate a scalar feature representing a pyrometer measurement of equivalent focal area. Using these scalar temperature features, coolant flow rate prediction errors of about nineteen percent were observed without covariates, and prediction errors of about six percent were observed with covariates. Second, to investigate the use of multiple point-based sensors, the feature selection from the thermal images was forced to successively smaller feature counts. Through this approach, a coolant flow rate prediction error of about seven percent was demonstrated using four temperature measurements as the sole inputs to the model (no covariate parameters required). These results indicate that a data-driven model can accurately predict \dot{m}_{cool} and T_{MGP} in a discrete turbine monitoring application using inputs of blade surface temperature.

Ultimately, knowledge of \dot{m}_{cool} and T_{MGP} allows for early detection and root-cause determination of temperature-induced degradation; these tasks are central to the efficacy of a condition-based operation and maintenance approach.

ACKNOWLEDGMENTS

This material is based upon work supported by the Department of Energy under Award Number DE-FE0031288. The authors would also like to recognize and thank Pratt & Whitney for supporting research presented in this paper.

This report was prepared as an account of work sponsored by an agency of the United States Government. Neither the United States Government nor any agency thereof, nor any of their employees, makes any warranty, express or implied, or assumes any legal liability or responsibility for the accuracy, completeness, or usefulness of any information, apparatus, product, or process disclosed, or represents that its use would not infringe privately owned rights. Reference herein to any specific commercial product, process, or service by trade name, trademark, manufacturer, or otherwise does not necessarily constitute or imply its endorsement, recommendation, or favoring by the United States Government or any agency thereof. The views and opinions of authors expressed herein do not necessarily state or reflect those of the United States Government or any agency thereof.

NOMENCLATURE

h	heat transfer coefficient
IR	infrared
k	thermal conductivity
L	material thickness
\dot{m}	mass flow rate
R	thermal resistance
RMSE	root mean square error
rpm	revolutions per minute
T	temperature (blade temperature when not accompanied by a subscript)
t	time
TBC	thermal barrier coating
x	streamwise direction on the blade pressure-side surface
z	pitchwise direction on the blade pressure-side surface
β	model coefficient
λ	LASSO tuning parameter

Subscripts

aw	adiabatic wall
cond	conduction heat transfer
conv	convection heat transfer
cool	pertaining to the blade coolant
f	external (hot) side of blade wall
ID	pertaining to the hardware radially-inward from the MGP
int	internal (cold) side of blade wall
max	maximum quantity across all measurements
meas	measured value
MGP	main gas path
OD	pertaining to the hardware radially-outward from the MGP
pred	predicted value
wall	blade wall

Operators

\bar{Q}	pitchwise-averaged quantity
$\bar{\bar{Q}}$	pitchwise- and streamwise-averaged quantity

REFERENCES

- [1] Meher-Homji, C. B., and Gabriles, G., 1998, "Gas Turbine Blade Failures - Causes, Avoidance, and Troubleshooting," *Proceedings of the 27th Turbomachinery Symposium*, pp. 129–180.
- [2] Bogard, D. G., and Thole, K. A., 2006, "Gas Turbine Film Cooling," *J. Propuls. Power*, **22**(2), pp. 249–270.
- [3] Han, J. C., and Wright, L. M., 2006, "Enhanced Internal Cooling of Turbine Blades and Vanes," *Gas Turbine Handbook*, p. 103.
- [4] Bunker, R. S., Dees, J. E., and Palafox, P., 2014, *Impingement Cooling in Gas Turbines: Design, Applications, and Limitations*, WIT Press.
- [5] Koff, B. L., 2004, "Gas Turbine Technology Evolution: A Designer's Perspective," *J. Propuls. Power*, **20**(4), pp. 577–595.
- [6] Winig, L., "GE's Big Bet on Data and Analytics," *MIT Sloan*.
- [7] Siemens Energy Inc., 2009, Siemens Operations and Maintenance Operating Cost Assessment Report.
- [8] Mathioudakis, K., Papathanasiou, A., Loukis, E., and Papailiou, K., 1991, "Fast Response Wall Pressure Measurement as a Means of Gas Turbine Blade Fault Identification," *J. Eng. Gas Turbines Power*, **113**, pp. 269–275.
- [9] Cox, J. R., Arnold, S. A., and Anusonti-Inthra, P., 2015, "Using Gas Turbine Engine Casing Accelerometer Measurements for Rotor Blade Health Monitoring," *51st AIAA/SAE/ASEE Joint Propulsion Conference*.
- [10] Goel, N., Kumar, A., Narasimhan, V., Nayak, A., and Srivastava, A., 2008, "Health Risk Assessment and Prognosis of Gas Turbine Blades by Simulation and Statistical Methods," *Canadian Conference on Electrical and Computer Engineering*, IEEE, pp. 1087–1091.
- [11] Hee, L. M., and Leong, M. S., "Improved Blade Fault Diagnosis Using Discrete Blade Passing Energy Packet and Rotor Dynamics Wavelet Analysis," GT2010-22218.
- [12] Rajagopalan, V., Behera, A., Bhattacharya, A., Prabhu, R., and Badami, V., 2012, "Estimation of Static Deflection under Operational Conditions for Blade Health Monitoring," *Prognostics and System Health Management Conference*.
- [13] Woike, M., Abdul-Aziz, A., and Clem, M., 2014, "Structural Health Monitoring on Turbine Engines Using Microwave Blade Tip Clearance Sensors," *Proceedings of SPIE Smart Sensor Phenomena, Technology, Networks, and Systems Integration*, p. 90620L-1-90620L-14.
- [14] Zhang, Z., Yang, G., and Hu, K., 2018, "Prediction of Fatigue Crack Growth in Gas Turbine Engine Blades Using Acoustic Emission," *Sensors*, **18**(5).
- [15] Kestner, B., Lieuwen, T., Hill, C., Angello, L., Barron, J., and Perullo, C. A., 2015, "Correlation Analysis of Multiple Sensors for Industrial Gas Turbine Compressor Blade Health Monitoring," *J. Eng. Gas Turbines Power*, **137**, pp. 112605-1-112605-11.
- [16] Yu, L., and Shrivastava, S., 2016, "Distributed Real Time Compressor Blade Health Monitoring System," *Proc. Annu. Conf. Progn. Heal. Manag. Soc.*, **8**(1).
- [17] Sridhar, V., and Chana, K. S., "Development of a Combined Eddy Current and Pressure Sensor for Gas Turbine Blade Health Monitoring," GT2017-63807.
- [18] Wu, S., Russhard, P., Yan, R., Tian, S., Wang, S., Zhao, Z., and Chen, X., 2020, "An Adaptive Online Blade Health Monitoring Method: From Raw Data to Parameters Identification," *IEEE Transactions on Instrumentation and Measurement*, pp. 2581–2592.
- [19] Chen, Z., Sheng, H., Xia, Y., Wang, W., and He, J., 2021, "A Comprehensive Review on Blade Tip Timing-Based Health Monitoring: Status and Future," *Mech. Syst. Signal Process.*, **149**.
- [20] Woike, M. R., Abdul-Aziz, A., and Bencic, T. J., 2010, "A Microwave Blade Tip Clearance Sensor for Propulsion Health Monitoring," *AIAA Infotech Aerospace Conference*.
- [21] Gubran, A. A., and Sinha, J. K., 2014, "Shaft Instantaneous Angular Speed for Blade Vibration in Rotating Machine," *Mech. Syst. Signal Process.*, **44**, pp. 47–59.
- [22] Urban, L., 1969, *Gas Turbine Engine Parameter Interrelationships*, HSD UTC, Windsor Locks, CT.
- [23] LeMieux, D. H., 2005, "On-Line Thermal Barrier Coating Monitoring for Real-Time Failure Protection and Life Maximization," <https://www.osti.gov/biblio/883320-line-thermal-barrier-coating-monitoring-real-time-failure-protection-life-maximization>.
- [24] Markham, J., Cosgrove, J., Scire, J., Haldeman, C., and Agoos, I., 2014, "Aircraft Engine-Mounted Camera System for Long Wavelength Infrared Imaging of in-Service Thermal Barrier Coated Turbine Blades," *Rev. Sci. Instrum.*, **85**, pp. 124902-1-124902-7.
- [25] Holanda, R., 1979, "Evaluation of Miniature Single-Wire Sheathed Thermocouples for Turbine Blade Temperature Measurement," NASA TM-79173.
- [26] Martin, L. C., and Holanda, R., 1994, "Applications of Thin-Film Thermocouples for Surface Temperature Measurement," *Conference on Spin-Off Technologies from NASA for Commercial Sensors and Scientific Applications*, pp. 65–76.
- [27] Schultz, D. L., and Jones, T. V., 1973, "Heat-Transfer Measurements in Short-Duration Hypersonic Facilities," AGARD, <https://apps.dtic.mil/sti/citations/AD0758590>.
- [28] Epstein, A. H., Guenette, G. R., Norton, R. J. G., and Yuzhang, C., 1986, "High-Frequency Response Heat-Flux

- Gauge,” *Rev. Sci. Instrum.*, **57**(4), pp. 639–649.
- [29] Dunn, M. G., and Haldeman, C. W., 2000, “Time-Averaged Heat Flux for a Recessed Tip, Lip, and Platform of a Transonic Turbine Blade,” *J. Turbomach.*, **122**(4), pp. 692–698.
- [30] Siroka, S., Foley, B. M., Berdanier, R. A., and Thole, K. A., 2021, “Application of 3-Omega Method for Thin-Film Heat Flux Gauge Calibration,” *Meas. Sci. Technol.*
- [31] Murugan, M., Walock, M., Ghoshal, A., Knapp, R., and Caesley, R., 2021, “Embedded Temperature Sensor Evaluations for Turbomachinery Component Health Monitoring,” *Energies*, **14**(852).
- [32] Nau, P., Yin, Z., Lammel, O., and Meier, W., 2019, “Wall Temperature Measurements in Gas Turbine Combustors With Thermographic Phosphors,” *J. Eng. Gas Turbines Power*, **141**, pp. 041021-1-041021-9.
- [33] Feist, J. P., Sollazzo, P. Y., Berthier, S., Charnley, B., and Wells, J., 2013, “Application of an Industrial Sensor Coating System on a Rolls-Royce Jet Engine for Temperature Detection,” *J. Eng. Gas Turbines Power*, **135**, pp. 012101-1-012101-9.
- [34] Chen, X., Mutasim, Z., Price, J., Feist, J. P., Heyes, A. L., and Seefeldt, S., 2005, “Industrial Sensor TBCs: Studies on Temperature Detection and Durability,” *Int. J. Appl. Ceram. Technol.*, **2**(5), pp. 414–421.
- [35] Atkinson, W. H., and Strange, R. R., “Turbine Pyrometry for Advanced Engines,” AIAA-87-2011.
- [36] Eggert, T., Schenk, B., and Pucher, H., 2002, “Development and Evaluation of a High-Resolution Turbine Pyrometer System,” *J. Turbomach.*, **124**(3), pp. 439–444.
- [37] Becker, W. J., Roby, R. J., O’Brien, W. F., and Bensing, G. K., 1994, “Dynamic Turbine Blade Temperature Measurements,” *J. Propuls. Power*, **10**(1), pp. 69–78.
- [38] Taniguchi, T., Sanbonsugi, K., Ozaki, Y., and Norimoto, A., “Temperature Measurement of High Speed Rotating Turbine Blades Using a Pyrometer,” GT2006-90247.
- [39] Brunner, M. H., Rose, M. G., Mühlbauer, K., and Abhari, R. S., 2007, “In-Engine Turbine Heat Transfer Measurement,” *Proc. Inst. Mech. Eng. Part A J. Power Energy*, **221**, pp. 727–734.
- [40] Lazzi Gazzini, S., Schädler, R., Kalfas, A. I., and Abhari, R. S., 2017, “Infrared Thermography with Non-Uniform Heat Flux Boundary Conditions on the Rotor Endwall of an Axial Turbine,” *Meas. Sci. Technol.*, **28**(025901).
- [41] Christensen, L., Celestina, R., Sperling, S., Mathison, R., Aksoy, H., and Liu, J., 2021, “Infrared Temperature Measurements of the Blade Tip for a Turbine Operating at Corrected Engine Conditions,” *J. Turbomach.*, **143**(10).
- [42] Knisely, B. F., Berdanier, R. A., Thole, K. A., Haldeman, C. W., Markham, J. R., Cosgrove, J. E., Carlson, A. E., and Scire, J. J., 2021, “Acquisition and Processing Considerations for Infrared Images of Rotating Turbine Blades,” *J. Turbomach.*, **143**, pp. 041013-1-041013-12.
- [43] Barringer, M. D., Coward, A., Clark, K. P., Thole, K. A., Schmitz, J., Wagner, J., Alvin, M. A., Burke, P., and Dennis, R., “The Design of a Steady Aero Thermal Research Turbine (START) for Studying Secondary Flow Leakages and Airfoil Heat Transfer,” GT2014-25570.
- [44] Berdanier, R. A., Monge-Concepción, I., Knisely, B. F., Barringer, M. D., Thole, K. A., and Grover, E. A., 2019, “Scaling Sealing Effectiveness in a Stator-Rotor Cavity for Differing Blade Spans,” *J. Turbomach.*, **141**(5), p. 051007.
- [45] Mori, M., Novak, L., and Sekavčnik, M., 2007, “Measurements on Rotating Blades Using IR Thermography,” *Exp. Therm. Fluid Sci.*, **32**(2), pp. 387–396.
- [46] Tibshirani, R., 1996, “Regression Shrinkage and Selection Via the Lasso,” *J. R. Stat. Soc. Ser. B*, **58**(1), pp. 267–288.
- [47] Cuccu, G., Danafar, S., Cudre-Mauroux, P., Gassner, M., Bernero, S., and Kryszczuk, K., 2017, “A Data-Driven Approach to Predict NOx-Emissions of Gas Turbines,” *IEEE International Conference on Big Data*, pp. 1283–1288.
- [48] Goyal, V., Xu, M., and Kapat, J., “Use of Vector Autoregressive Model for Anomaly Detection in Utility Gas Turbines,” GT2019-90995.
- [49] Olsson, T., Ramentol, E., Rahman, M., Oostveen, M., and Kyprianidis, K., 2021, “A Data-Driven Approach for Predicting Long-Term Degradation of a Fleet of Micro Gas Turbines,” *Energy AI*, **4**, p. 100064.
- [50] Coad, A., and Srhoj, S., 2020, “Catching Gazelles with a Lasso: Big Data Techniques for the Prediction of High-Growth Firms,” *Small Bus. Econ.*, **55**, pp. 541–565.
- [51] “Thermocouple Types” [Online]. Available: <https://www.omega.com/en-us/thermocouple-types>.